

Designing electrolytes with high solubility of sulfides/disulfides for high-energy-density and low-cost K-Na/S batteries

Received: 20 June 2023

Accepted: 19 August 2024

Published online: 05 September 2024

 Check for updates

Liying Tian^{1,2,6}, Zhenghao Yang^{1,6}, Shiyi Yuan¹, Tye Milazzo³, Qian Cheng¹, Syed Rasool¹, Wenrui Lei¹, Wenbo Li¹, Yucheng Yang¹, Tianwei Jin¹, Shengyu Cong¹, Joseph Francis Wild¹, Yonghua Du¹,⁵, Tengfei Luo¹,³, Donghui Long¹,² & Yuan Yang¹

Alkaline metal sulfur (AMS) batteries offer a promising solution for grid-level energy storage due to their low cost and long cycle life. However, the formation of solid compounds such as M_2S_2 and M_2S ($M = Na, K$) during cycling limits their performance. Here we unveil intermediate-temperature K-Na/S batteries utilizing advanced electrolytes that dissolve all polysulfides and sulfides (K_2S_x , $x = 1-8$), significantly enhancing reaction kinetics, specific capacity, and energy density. These batteries achieve near-theoretical capacity (1655 mAh g⁻¹ sulfur) at 75 °C with a 1 M sulfur concentration. At a 4 M sulfur concentration, they deliver 830 mAh g⁻¹ at 2 mA cm⁻², retaining 71% capacity after 1000 cycles. This new K-Na/S battery with specific energy of 150-250 Wh kg⁻¹ only employs earth-abundant elements, making it attractive for long-duration energy storage.

Grid-level energy storage is important for addressing climate change and realizing a sustainable future^{1,2} since it can stabilize intermittent power generation from renewable solar and wind energy³. Long-duration energy storage (LDES) with an operational period over one day is of particular importance as it enables stable power output under extreme conditions and leverages seasonal variations⁴⁻⁶. However, LDES is highly challenging due to the demanding requirement on low cost⁷, since it is operated for a limited number of cycles⁸, such as ~1500 times for weekly operation and ~400 times for monthly operation in 30 years, which is much less than short-term energy storage with everyday cycling and thus ~10,000 cycles in 30 years^{9,10}.

Na/S and K/S batteries are promising for LDES since all elements involved are earth-abundant and inexpensive¹¹⁻¹⁴. High-temperature (HT) Na/S batteries operated at 300–350 °C have been commercialized, which use β'' -alumina solid electrolytes (BASE) to separate the sulfur cathode and the Na anode^{15,16}. The full cell reaction is $2 Na + x S \rightarrow Na_2S_x$ ($x = 3-5$) with an average voltage of 2.0 V^{17,18}. Although the HT Na/S battery offers a high theoretical energy density and a long cycle

life¹⁹, its high operating temperature causes substantial challenges such as corrosion and thermal management²⁰. On the other end, room-temperature (RT) Na/S and K/S batteries use liquid organic electrolytes to mitigate these issues²¹⁻²³, but encounter new challenges such as strong polysulfide shuttling, metal dendrites, and poor sulfur utilization²⁴⁻²⁸. The cell voltage also decreases to 1.2–1.5 V²⁹.

Intermediate-temperature (IT) Na/S and K/S batteries, which function at 100–150 °C, are receiving increasing attention because they take advantage of their HT and RT counterparts^{30,31}. IT Na/S and K/S batteries use BASE to fully prevent polysulfide shuttling and greatly suppress metal dendrites, and organic liquid electrolytes (e.g., tetraglyme/TEGDME) at the cathode side to enhance kinetics^{17,32}.

A common challenge for all HT/IT/RT Na/S and K/S batteries is the formation of solid M_2S_2 and M_2S ($M = Na, K$) with ultralow ionic diffusivity in discharge³³, which limits the specific capacity of the cathode to only ~500 mAh g⁻¹ for Na/S and ~400 mAh g⁻¹ for K/S, which corresponds to only M_2S_4/M_2S_3 ^{31,34,35}. Limited outliers report initial capacities at 600–800 mAh/g, but they either use excessive matrix such as

¹Department of Applied Physics and Applied Mathematics, Columbia University, New York, NY, US. ²Key Laboratory of Chemical Engineering, East China University of Science and Technology, Shanghai, China. ³Department of Aerospace and Mechanical Engineering, University of Notre Dame, Notre Dame, IN, US. ⁴Department of Chemistry, Columbia University, New York, NY, US. ⁵National Synchrotron Light Source II, Brookhaven National Laboratory, Upton, NY, US. ⁶These authors contributed equally: Liying Tian, Zhenghao Yang.  e-mail: tluo@nd.edu; longdh@mail.ecust.edu.cn; yy2664@columbia.edu

polyacrylonitrile (PAN)³⁶ or show fast capacity decay³⁷ (Supplementary Note 1). To address this issue and substantially enhance discharge capacity, here we propose a new family of amide electrolytes that show reasonable solubility of M_2S_2/M_2S (e.g., 1.2 M), which drastically enhances ionic diffusivity and reaction kinetics on the cathode side. We apply this new design principle to IT K-Na alloy/S batteries (K-Na/S for short) in this work because 1) BASE in IT can eliminate the shuttle effect caused by such a high solubility, and 2) IT K-Na/S batteries have a higher average voltage of ~2.1 V than 1.2–1.5 V in RT Na/S and K/S batteries. 3) The high solubility can also substantially lower the operation temperature from 150 °C in reported IT Na/S and K/S batteries to 50–100 °C.

Specifically, an acetamide/ε-caprolactam (CPL) eutectic solvent is used, which can dissolve K_2S up to 1.43 M at 75 °C and has a lower melting point (~8 °C) than acetamide (82 °C) and CPL (71 °C)³⁸. With such a new electrolyte, a K-Na alloy/ K^+ -conducting BASE (K-BASE)/1 M [S] battery can reach a nearly theoretical discharge capacity of 1655 mAh g⁻¹ sulfur at 75 °C. When [S] reaches 4 M, the specific capacity still remains at 830 mAh g⁻¹ sulfur at 2 mA cm⁻² with a capacity retention of 71 % after 1000 cycles. A discharge capacity of 703 mAh g⁻¹ sulfur is also achieved at [S] of 8 M. Note that [S] counts sulfur from all polysulfides and sulfides inside the solution. These values correspond to specific energies of 150–250 Wh kg⁻¹ at the cell level with BASE and packaging considered. Given the earth abundance of all elements involved, this system has the potential to achieve attractive cost and performance for LDES.

Results

Design principle of K-Na/S batteries with soluble sulfides and disulfides

The cathode is polysulfide dissolved in a mixture of CPL and acetamide (with 1:1 molar ratio, Fig. 1a, since it has the lowest melting point). Therefore, the cathode reaction in the range of S_3^{2-}/S^{2-} is $2S_3^{2-}(l) + 2e^- \rightarrow 3S_2^{2-}(l)$ and $S_2^{2-}(l) + 2e^- \rightarrow 2S^{2-}(l)$ instead of $2S_3^{2-}(l) + 2e^- + 6K^+ \rightarrow 3K_2S_2(s)$ and $K_2S_2(s) + 2e^- + 2K^+ \rightarrow 2K_2S(s)$ in conventional ether electrolytes. Such soluble redox significantly boosts reaction kinetics as the sluggish diffusion in solids is avoided. This catholyte is separated

from a K-Na liquid alloy anode (1:1) by a commercial K-BASE, which does not conduct Na^{+} ³¹. The liquid alloy anode is used to reduce the anode/K-BASE interfacial impedance^{39–41}. Therefore, the full cell reaction is $S + 2K \rightarrow K_2S$.

The energy density of such a system depends on the concentration of sulfur. Based on the theoretical specific capacity of sulfur (1675 mAh g⁻¹) and K (687 mAh g⁻¹), the theoretical specific energy reaches 95.8, 295, and 452 Wh kg⁻¹ at 1 M, 4 M and 8 M sulfur, respectively, with the mass of sulfur, liquid electrolyte and anode considered (Fig. 1b). When masses of BASE and packaging are included, the cell-level specific energy is expected to reach 136 and 186 Wh kg⁻¹ at 4 M and 8 M sulfur, respectively (24 h discharge), and 179 and 276 Wh kg⁻¹ at 4 M and 8 M sulfur (one week discharge), respectively. It should be noted that the calculation is only for materials themselves and the N/P ratio of 1, while the dependence of energy density on the N/P ratio is shown in Supplementary Fig. 1. Details can be found in Supplementary Note 2.

Dissolution behavior in the CPL/acetamide mixture

To validate our new design, we first test the solubility of K_2S_x in CPL/acetamide. This mixed solvent readily dissolves K_2S_8 , K_2S_4 , K_2S_2 , and K_2S with 1.2 M [S] at 25 °C (Fig. 2a), meanwhile being transparent and allowing light to pass straightly (Fig. 2b). In contrast, the solubility of K_2S in a conventional TEGDME electrolyte is less than 0.1 M at 25 °C, as reflected by the milky appearance of its suspension (Fig. 2b). Further temperature-dependent solubility tests show that the solubilities of K_2S_2/K_2S are 1.44 M/1.40 M at 60 °C, 1.50 M/1.43 M at 75 °C, 1.64 M/1.47 M at 100 °C and 1.72 M/1.50 M at 120 °C, respectively (Fig. 2c). As the length of polysulfide increase, the solubility even goes higher (Fig. 2d). The solubility for CPL/acetamide with other mixing ratios are also tested and shown in Supplementary Fig. 2. Such high solubilities suggest that the electrochemical reaction in discharge involves soluble sulfide (S_2^{2-}) and polysulfide ions (S_x^{2-}) instead of solid K_2S and K_2S_x , which is expected to significantly enhance ionic diffusion and reaction kinetics⁴².

Molecular dynamics (MD) simulations were conducted to better understand the different dissolution behaviors of K_2S in CPL/

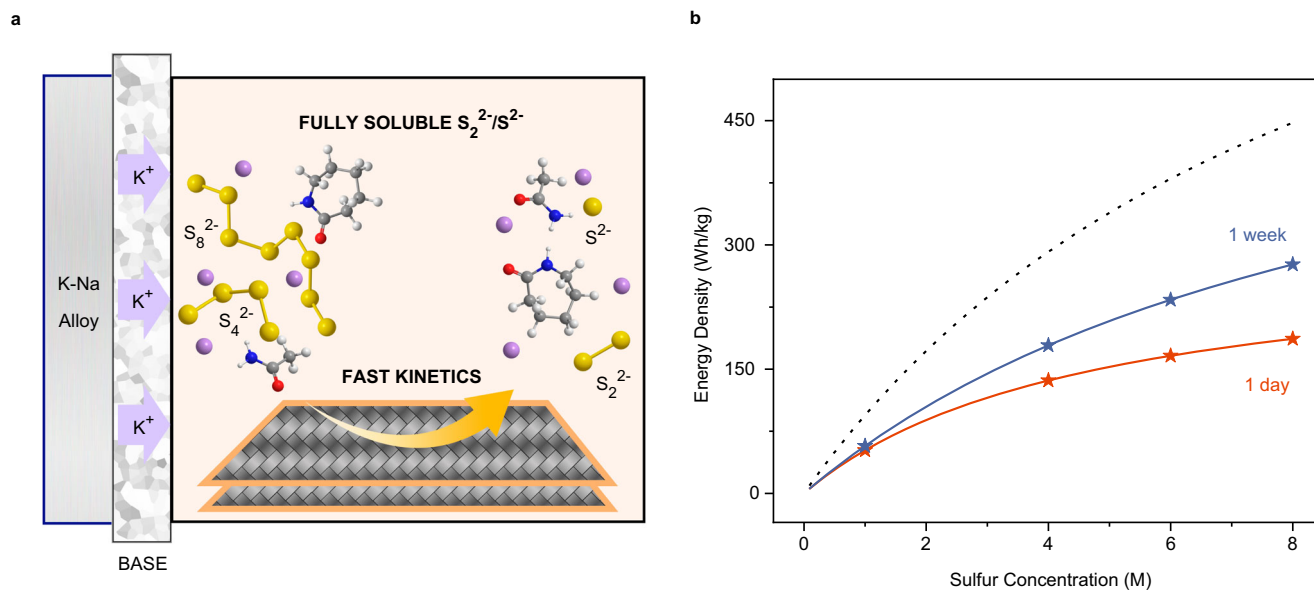


Fig. 1 | The proposed K-Na/S battery with its specific energy. **a** A schematic of the proposed K-Na/S battery. The liquid K-Na alloy anode wets K-BASE well, leading to low anode/solid electrolyte interfacial impedance. K-BASE only conducts K^+ but not Na^+ , so the mechanism is of K/S batteries. The acetamide/CPL solvent dissolves K_2S_x ($x = 1–8$), which promotes ionic transport in K_2S_2 and K_2S , and thus reaction kinetics

and specific capacity. The synergy of these two strategies leads to K/S batteries with high energy density even at 75 °C. **b** The concentration dependence of theoretical (dash line) and practical energy densities of the proposed K-Na/S battery. Blue and red lines are for discharge times of 1 week and 1 day, respectively.

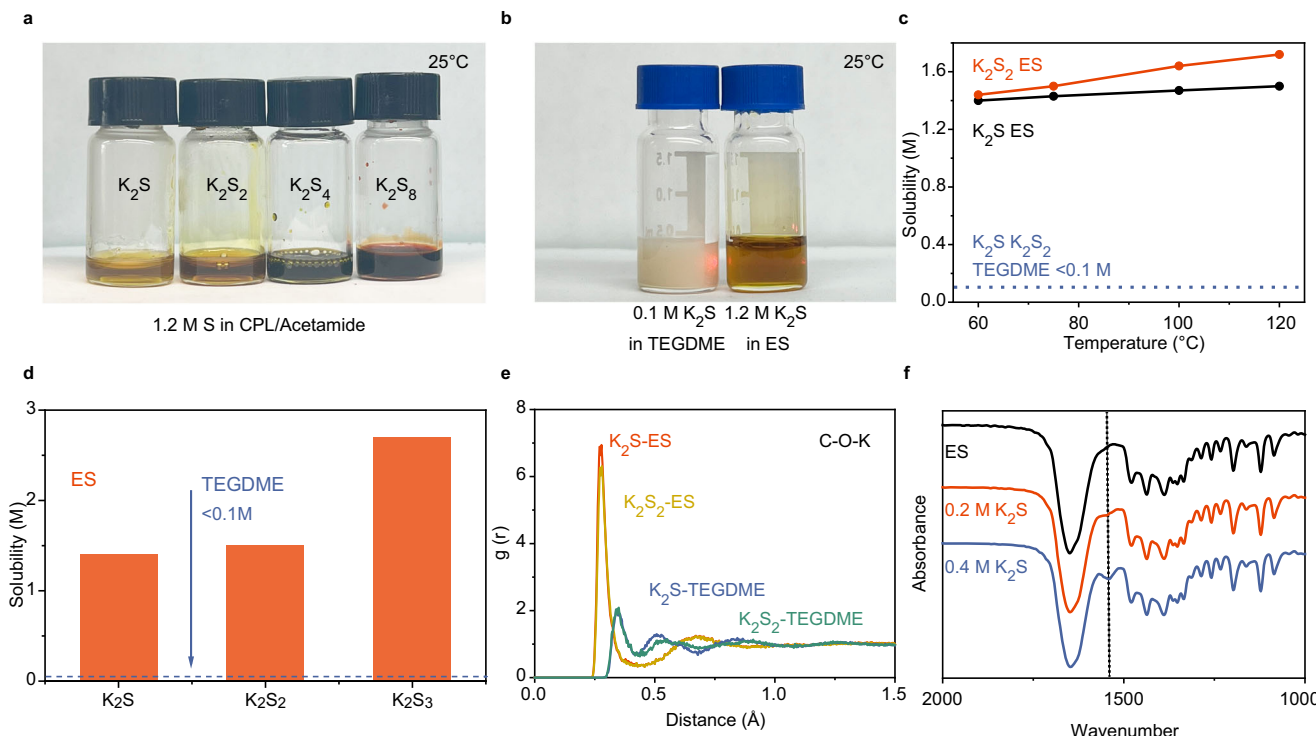


Fig. 2 | Solubility tests and dissolution mechanisms of disulfides and sulfides in the CPL/acetamide mixed solvent. **a** The dissolution behavior of K_2S_x ($x = 1, 2, 4, 8$) in CPL/acetamide at 25 °C. The concentrations of sulfur in all samples are 1.2 M. **b** Tyndall effect tests for 1.2 M K_2S in CPL/acetamide eutectic solvent (ES) and 0.1 M K_2S in TEGDME, excluding the possibility of forming colloids in ES. **c** Solubilities of K_2S and K_2S_2 in ES and TEGDME from 60 °C to 120 °C. **d** Solubilities of K_2S , K_2S_2 , and

K_2S_3 in ES and TEGDME in 75 °C. **e** Calculated radial distribution function of molecular dynamics (MD) simulations of K_2S and K_2S_2 in ES and TEGDME. The larger peak height in ES indicates stronger bonding between K^+ and ES. **f** Fourier Transform Infrared Spectroscopy (FTIR) spectra of pure ES and 0.2 M/0.4 M K_2S in ES. A peak representing K^+ – solvent interaction shows up at 1550 cm^{-1} with an increasing concentration of K_2S .

acetamide and TEGDME (Supplementary Fig. 3 and Supplementary Note 3). MD results show that the free energy of K^+ and S^{2-} when dissolved in CPL/acetamide is -5.2 kJ mol^{-1} compared to the state where these ions are in a vacuum, while in TEGDME, this value is $199.6 \text{ kJ mol}^{-1}$. This clearly indicates that K_2S is significantly more soluble in CPL/acetamide than TEGDME. To explore the molecular level origin of this trend, we compared radial distribution functions (RDF) of the dissolved ions around the polar groups in CPL/acetamide and TEGDME. The K-O peak in CPL/acetamide exhibited a much higher first peak compared to that in TEGDME, and the position of the first peak in CPL/acetamide is at a shorter distance ($\sim 0.27 \text{ \AA}$) than in TEGDME ($\sim 0.36 \text{ \AA}$). This indicates that the C=O group in CPL/acetamide has a stronger interaction towards K^+ and can attract more K^+ ions closer to the O atom in CPL/acetamide than in TEGDME (Fig. 2e), which contributes to the dissolution of K_2S .

Such simulation results are also consistent with FTIR results (Fig. 2f). As the concentration of K_2S increases, a characteristic peak appeared at 1550 cm^{-1} , next to the C=O bond at 1650 cm^{-1} . This peak arises from the interaction between K^+ and the C=O bond⁴³. Furthermore, MD RDF for other ion/polar group pairs also shows stronger interaction in CPL/acetamide than TEGDME (Supplementary Fig. 4).

K-Na/S Batteries with 1 M [S] in CPL/acetamide

To demonstrate that high solubilities of K_2S_2/K_2S in CPL/acetamide can enhance the discharge capacity, we assembled K-Na alloy/K-BASE/polysulfide catholyte coin cells with carbon fiber papers as the cathode current collector. The CPL/acetamide solvent is stable between 1.3 and 3.0 V vs. $K^+/K\text{-Na}$ (1:1) (Supplementary Fig. 5). The amount of catholyte corresponds to 1.41 mAh cm^{-2} at 1 M [S], 5.64 mAh cm^{-2} at 4 M [S] and 11.3 mAh cm^{-2} at 8 M [S] with the theoretical capacity of sulfur assumed.

On the anode side, 1.25 wt% carbon black (CB) was added to the K-Na alloy (1:1), which reduces the interfacial impedance of K-Na alloy/BASE from $\sim 21 \text{ \Omega}$ without CB to $\sim 7 \text{ \Omega}$ with CB (Supplementary Figs. 6 and 7a). In K-Na/BASE/K-Na symmetric cells, the overpotential reduces from $\sim 40 \text{ mV}$ without CB to $\sim 20 \text{ mV}$ with CB at 2.6 mA cm^{-2} (Fig. 3a), and the critical current density increases from 40 mA cm^{-2} without CB to 70 mA cm^{-2} with CB (Supplementary Fig. 7b and Supplementary Note 4).

We first test cells with 1 M [S] catholyte where K_2S_2/K_2S are fully soluble. At 0.5 mA cm^{-2} (0.35 C, 1 C = 1675 mA g^{-1}), the first discharge plateaus (2.1 – 2.7 V) in both CPL/acetamide and TEGDME electrolyte overlap well, reflecting good kinetics of S/S_4^{2-} in both electrolytes (Fig. 3b). However, a sudden drop was observed in TEGDME at $\sim 600 \text{ mAh g}^{-1}$ sulfur, due to formation of solid K_2S_2/K_2S with low diffusivity and poor kinetics. The capacity reaches 630 mAh g^{-1} in cycle 33, and 567 mAh g^{-1} in cycle 100, which corresponds to a capacity retention of 90% or 99.84% /cycle from cycle 33 to 100.

On the other hand, the cell with CPL/acetamide shows high discharge specific capacities of 1591 mAh g^{-1} sulfur in cycle 2 and 1655 mAh g^{-1} in cycle 7, which are almost the same as the theoretical value of 1675 mAh g^{-1} (Fig. 3c). The capacity remains at 1263 mAh g^{-1} after 300 cycles, corresponding to a capacity retention of 76.3%, or 99.91% /cycle (Fig. 3c). These results obviously reflect that the soluble nature of K_2S_2/K_2S in CPL/acetamide dramatically improves reaction kinetics and thus enhances the discharge capacity.

We further performed electrochemical impedance spectroscopy (EIS) to understand how solubility affects electrochemical performance. At full charge (Fig. 3d), impedances of cells with TEGDME and CPL/acetamide are both low, since the redox of high-order polysulfides is kinetically fast. Moreover, the diffusion tails are both negligible, indicating fast diffusion in the liquid phase. On the other side, at

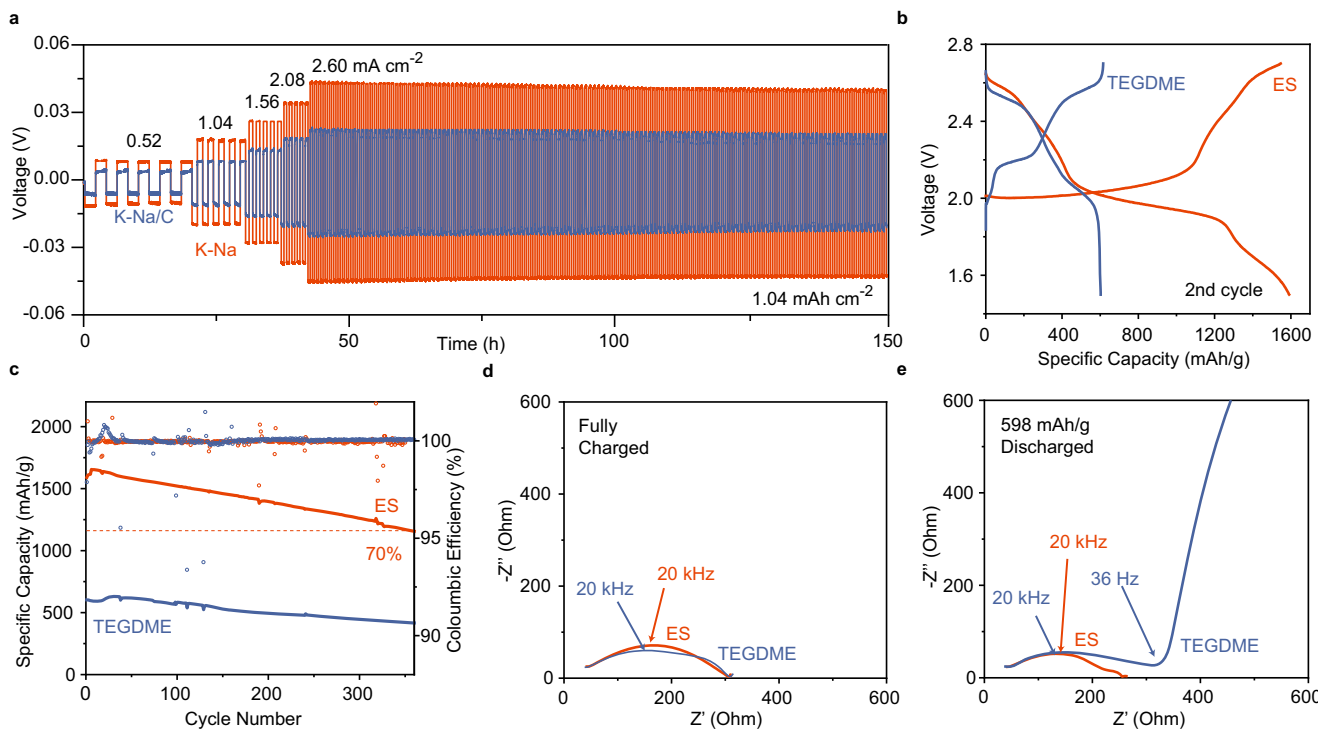


Fig. 3 | Electrochemical performance of K-Na/S batteries with 1 M sulfur in catholytes. **a** Cycling of K-Na/BASE/K-Na symmetric cells with carbon black (blue) and without carbon black (orange) at different current densities. **b** Charge/discharge voltage profiles of 1 M [S] cells in CPL/acetamide eutectic solvent (ES) and TEGDME electrolyte, respectively. The initial composition is Na_2S_8 , with K^+ ions

passing BASE. **c** Cycling performance of cells with ES and TEGDME electrolytes at 0.5 mA cm^{-2} . Electrochemical impedance spectroscopy of cells at **(d)** the fully charged state, and **(e)** discharged to 598 mAh g^{-1} sulfur, corresponding to $\text{M}_2\text{S}_{2.8}$. The range of frequency is $1 \text{ MHz} - 1 \text{ mHz}$. All tests are done at 75°C in an oven.

598 mAh g^{-1} , which corresponds to $\text{M}_2\text{S}_{2.8}$ and 99.1 % of the full discharge capacity in TEGDME, the cell with TEGDME shows a long diffusion tail with a diffusivity of $\sim 8 \times 10^{-16} \text{ cm}^2 \text{ s}^{-1}$, validating poor ionic transport in solid $\text{K}_2\text{S}_2/\text{K}_2\text{S}$. However, the diffusion tail in CPL/acetamide is still negligible (Fig. 3e). Further ionic conductivity measurements indicate that the diffusivity is $\sim 3 \times 10^{-7} \text{ cm}^2 \text{ s}^{-1}$ in the liquid phase (Supplementary Note 5).

To verify the absence of solid precipitation in CPL/acetamide, several characterization methods were applied to elucidate the precipitation dynamics. First, ex-situ scanning electron microscope (SEM) images of the cathode at 1.5 V revealed a smooth carbon surface without noticeable solid precipitates in CPL/acetamide (Fig. 4a). Moreover, S and K signals are very weak in Energy Dispersive Spectroscopy (EDS) spectrum, and their ratio corresponds to $\text{K}_2\text{S}_{1.0}$, proving the full transformation from sulfur to K_2S . In contrast, in TEGDME cells, there are plenty of micron-sized particles, and EDS indicates that their compositions are $\text{K}_2\text{S}_{2.8}$ (Fig. 4b and Supplementary Fig. 8), corresponding to the discharge ending capacity of 562 mAh g^{-1} ($\text{K}_2\text{S}_{3.0}$). The same results are also observed by ex-situ Synchrotron-based X-ray Absorption. Near Edge Structure (XANES) mapping of sulfur shows that the intensities of sulfur signals in CPL/acetamide after 1 and 10 cycles are less than 1/10 of those in TEGDME, indicating no or very little solid precipitation (Fig. 4c).

Operando optical imaging further supports that there is indeed no solid precipitation with the CPL/acetamide catholyte even at the end of discharge at 25°C (1500 mAh g^{-1} , Fig. 4e and Supplementary Video 1 and 3). In contrast, in TEGDME, precipitation begin to appear as early as 513 mAh g^{-1} ($\text{K}_2\text{S}_{3.3}$, Fig. 4f and Supplementary Video 2), and granular solid precipitates exist everywhere over carbon fibers at the end of discharge (609 mAh g^{-1} , $\text{K}_2\text{S}_{2.8}$, Fig. 4f and Supplementary Video 4). These imaging results clearly show that high solubility of K_2S_2

and K_2S can avoid solid precipitation and greatly extend the discharge range of sulfur cathode in K-Na/S batteries.

K-Na/S Batteries with 4 M and 8 M [S] in CPL/acetamide

We further test samples with 4 M and 8 M [S] to enhance the energy density of K-Na/S batteries. As [S] is higher than the solubility of K_2S_2 and K_2S , the cathode reaction involves solid formation such as $2\text{S}_3^{2-}(\text{l}) + 2\text{e}^- + 6\text{K}^+ \rightarrow 3\text{K}_2\text{S}_2(\text{s})$ and $\text{K}_2\text{S}_2(\text{l}) + 2\text{e}^- + 2\text{K}^+ \rightarrow 2\text{K}_2\text{S}(\text{s})$, which further contributes to cell capacity in parallel with liquid/liquid transformation among $\text{S}_3^{2-}/\text{S}_2^{2-}/\text{S}^{2-}$.

At 0.5 mA cm^{-2} (0.09 C), the 4 M [S] cell in CPL/acetamide shows an initial discharge capacity of 913 mAh g^{-1} , which increases gradually to 1106 mAh g^{-1} at cycle 46 and remains at 1086 mAh g^{-1} (98.2%) after 100 cycles. Such capacity corresponds to $\sim 3.9 \text{ mAh cm}^{-2}$ (Fig. 5 a, b). The average coulombic efficiency (CE) is 100.2% from cycle 1 to 100, indicating no shuttle effect or noticeable side reactions. The gradual capacity increase in CPL/acetamide upon cycling probably comes from better wetting between the catholyte and the carbon substrate, which is supported by decreasing charge transfer resistance upon cycling (Supplementary Fig. 9). In contrast, 4 M [S] in TEGDME only gives an initial discharge capacity of 467 mAh g^{-1} , which remains at 439 mAh g^{-1} after 100 cycles (94.0 %). The corresponding average CE is 100.1%.

When [S] further increases to 8 M, the cell in CPL/acetamide shows an initial discharge capacity of 411 mAh g^{-1} , which gradually increases to 672 mAh g^{-1} after 100 cycles (Fig. 5b). The average CE is 100.5 % from cycle 1 to 100. The increasing capacity is likely a result of improved wetting during cycling since 8 M [S] in ES is viscous. The increasing capacity is probably the reason for CE exceeding 100%, as more and more capacity can be utilized during cycling. On the other hand, 8 M [S] in TEGDME only gives an initial discharge capacity of 432 mAh g^{-1} , which remains at 424 mAh g^{-1} after 100 cycles.

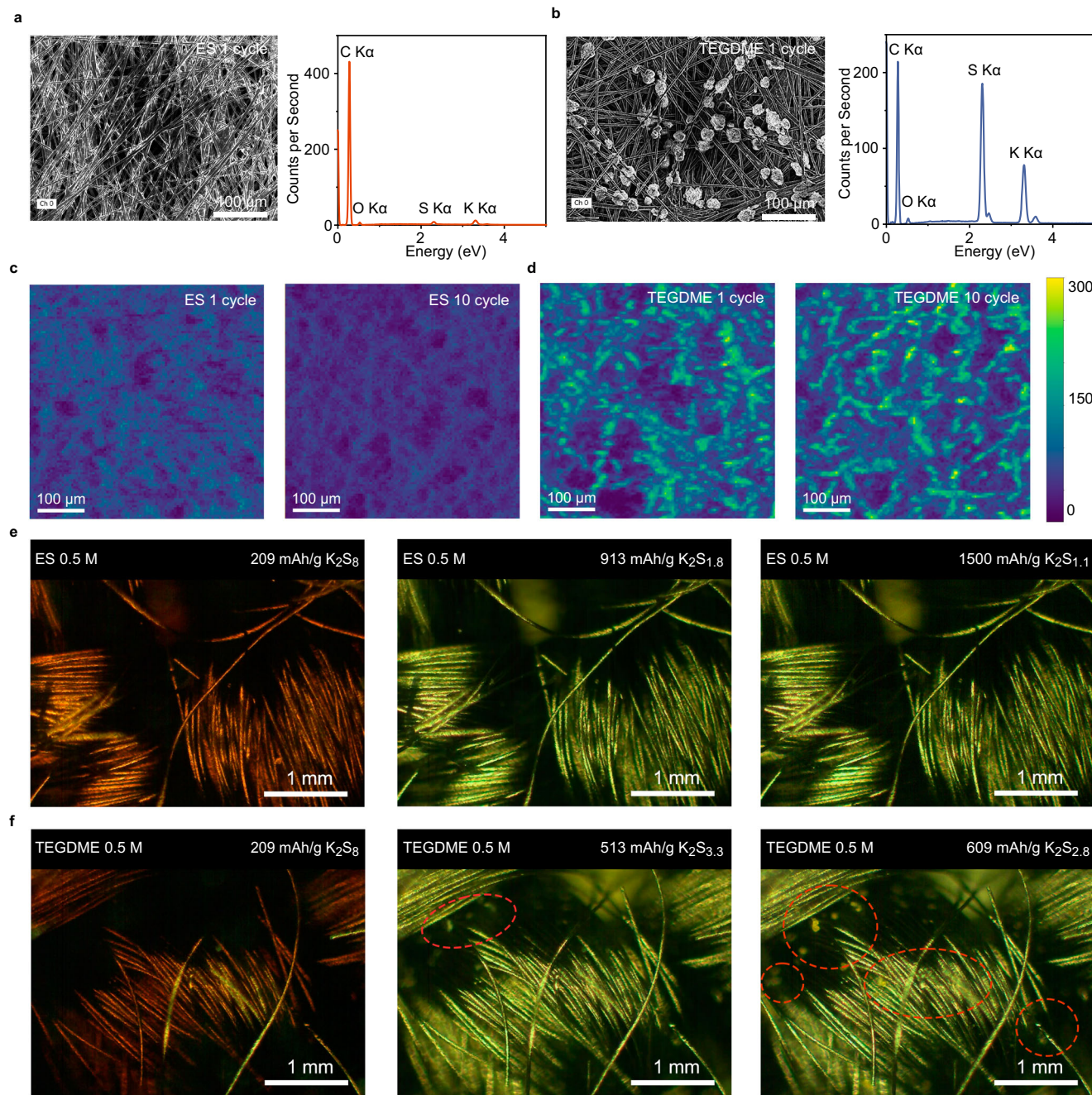


Fig. 4 | Observation of K_2S_x particles in cathode side of K-Na/S batteries. **a, b** Scanning Electron Microscope (SEM) imaging and Energy Dispersive Spectroscopy (EDS) spectrum results of carbon paper from cells after the first cycle with 1 M [S] CPL/acetamide eutectic solvent (ES) (**a**) and TEGDME (**b**). **c, d** X-ray Absorption Near Edge Structure (XANES) mapping of sulfur element for carbon paper from cells after 1 or 10 cycles with ES (**c**) and TEGDME (**d**). **e, f** *Operando*

optical microscope imaging of catholyte at room temperature in (**e**), ES where no precipitation is observed even at the end of discharge and (**f**), TEGDME where precipitation starts to appear in the middle of discharge. Precipitates are marked by red dashed circles. [S] in the catholyte and temperature are 1 M and 75 °C, respectively, for (**a-d**), and 0.5 M and 25 °C, respectively, in (**e**) and (**f**).

Such results also echo with impedance data. Again, no significant diffusion tail is observed at full charge due to fast kinetics (Fig. 5f). However, a long diffusion tail is observed at the end of discharge in TEGDME with an estimated diffusivity of $9 \times 10^{-14} \text{ cm}^2 \text{ s}^{-1}$. This higher diffusivity than that number in Fig. 3f may arise from a lower discharge capacity with 4 M sulfur, which corresponds to a higher order of polysulfides. On the other hand, the diffusion tail remains negligible in CPL/acetamide, indicating that even if solid $\text{K}_2\text{S}_2/\text{K}_2\text{S}$ is formed in CPL/acetamide, the presence of soluble $\text{K}_2\text{S}_2/\text{K}_2\text{S}$ still helps enhance ionic diffusion and discharge capacity significantly.

We further demonstrate long-term cycling at 2 mA cm^{-2} (0.38 C) in 4 M [S] cells, which corresponds to a discharge time of 1.3 h. The initial discharge capacity is 830 mAh g^{-1} , which remains at 712 mAh g^{-1} (86%) after 500 cycles, 593 mAh g^{-1} (71%) after 1000 cycles, and 505 mAh g^{-1} (61%) after 1500 cycles. The variation in CE comes from environment disturbance, which happens averagely once every ~50 cycles (10 days, Supplementary Fig. 10). In contrast, the TEGDME cell only has an initial specific capacity of 378 mAh g^{-1} at 2 mA cm^{-2} , which remains at 343 mAh g^{-1} after 1000 cycles. The reason for better retention of TEGDME cells is discussed in Supplementary Note 6. Such

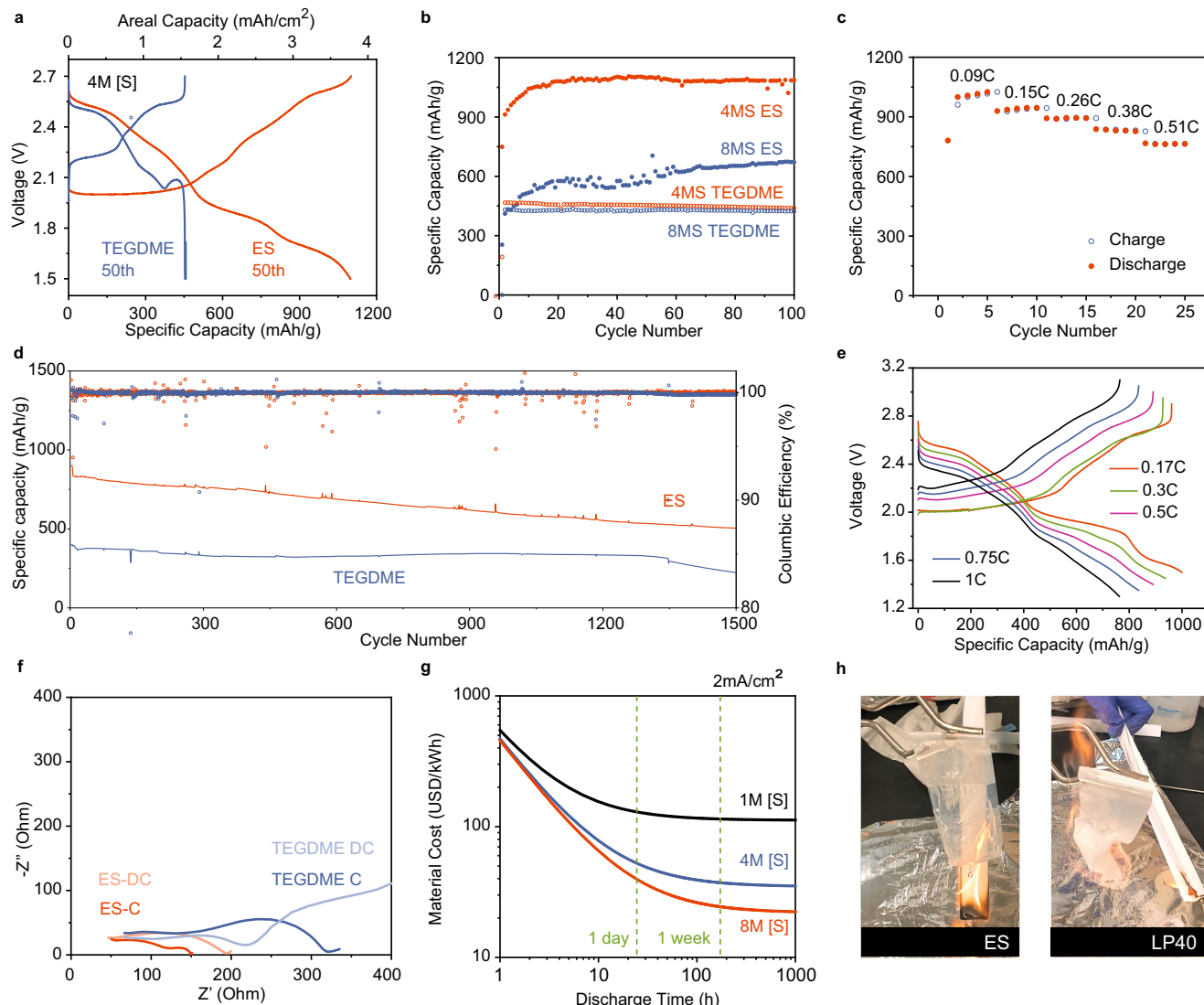


Fig. 5 | Electrochemical performance of K-Na/S batteries with 4 M and 8 M sulfur in catholytes. **a** Charge/discharge voltage profiles of cells with 4 M sulfur in CPL/acetamide eutectic solvent (ES) and TEGDME catholyte. The current densities are 0.5 mA cm^{-2} (0.09 C). **b** Cycling performance of cells with sulfur concentrations of 4 M and 8 M [S] in the cathode. The current densities are 0.5 mA cm^{-2} . **c** Rate performance of cells with 4 M sulfur in ES electrolyte and TEGDME electrolyte. **d** Cycling performance of cells with 4 M sulfur in the cathode at 2 mA cm^{-2} . The first 5 cycles are at 0.5 mA cm^{-2} . **e** Charge/discharge voltage profiles of cells with various

C-rates. **f** Electrochemical impedance spectroscopy of cells with 4 M sulfur in the cathode at the fully charged state (C) and at a discharge capacity of 460 mAh g^{-1} sulfur (DC). The electrolytes are ES and TEGDME, respectively. **g** The discharge time dependence of material cost for K-Na/S battery with 1 M [S] / 4 M [S] / 8 M [S] at 2 mA cm^{-2} . **h** Eutectic solvent with a separator (ES, left) and conventional Li-ion battery electrolyte with a separator (LP40, right) on fire. Samples with polysulfides inside can be found in Supplementary Video 5. All electrochemical tests for **a-f** are done in a 75°C oven.

superior capacity further confirms that the high solubility of $\text{K}_2\text{S}_2/\text{K}_2\text{S}$ in CPL/acetamide helps enhance kinetics and increase energy density even at a concentration of sulfur beyond solubility. The cycling performance of cells with CPL/acetamide is also promising for practical LDES.

The K-Na/S cell with 4 M [S] in CPL/acetamide also shows reasonable power capability. At 0.5 mA cm^{-2} (0.09 C), the discharge capacity is 1025 mAh g^{-1} , and it remains at 895 and 765 mAh g^{-1} at 1.5 mA cm^{-2} (0.26 C) and 2.5 mA cm^{-2} (0.51 C), respectively (Fig. 5c and e). For comparison, the specific capacities of TEGDME catholyte counterparts are around 430 mAh g^{-1} between $0.5\text{--}2.5 \text{ mA cm}^{-2}$. Impedance data show that the contribution from BASE, K-Na/BASE interface, and cathode are 15Ω , 19Ω , and 122Ω at the end of discharge, respectively (Fig. 5f). This suggests that cathode impedance is the main limiting factor for power capability, which can be further reduced by increasing the surface area of current collector, or

surface modifications to enhance wetting between $\text{K}_2\text{S}_2/\text{K}_2\text{S}$ and the carbon substrate.

Besides electrochemical performance, we also further perform preliminary experiments to understand the thermal stability of CPL/acetamide electrolytes. Acetamide and CPL have melting points of 80 and 69°C , respectively, indicating that they both have low vapor pressure compared to common carbonate and ether electrolytes and reasonable thermal stability at $60\text{--}120^\circ\text{C}$. We also put CPL/acetamide on fire from ignited paper with and without polysulfides inside (Fig. 5h and Supplementary Video 5 and 6), and these liquids did not catch fire in both cases. These results indicate that such electrolytes have reasonable thermal stability and are promising for grid-scale energy storage.

Discussion

We further estimate the cost at the cell level, including all components (electrolytes, BASE, electrode materials, and packaging), and the

details can be found in Supplementary Note 7⁴⁴. Based on 2 mA cm⁻² and a discharge time of 24 h, the materials costs are \$54 and \$41 kWh⁻¹ for 4 and 8 M sulfur, respectively. When the discharge time increases to one week, the cell-level materials costs are further reduced to \$39 and \$26 kWh⁻¹ for 4 and 8 M sulfur, respectively (Fig. 5g). With a higher current density of 5 mA cm⁻², the material cost can be further reduced by 3–8% (Supplementary Fig. 11). Such low costs are attributed to inexpensive active materials⁴⁵.

In addition, manufacturing costs should also be considered. Although this is difficult to evaluate, it is likely to be on par with or less than Li-ion batteries⁴⁶. This is because no slurry coating or drying is needed for alkaline metal sulfur batteries, which count for the majority part of manufacturing cost in Li-ion batteries⁴⁷. On the other hand, Na and K need to be handled in an air-free environment.

Beside K-Na/S batteries, the same design principle can also be applied to Na/S batteries as Na₂S and Na₂S₂ also have solubilities of 1.85 M and 2.80 M in CPL/acetamide at 75 °C, respectively. We also see a high discharge capacity of 940 mAh/g in the first cycle (Supplementary Fig. 12). The cycling performance needs to be improved due to poor interfaces between Na metal and BASE at 75 °C. We will report this in the future.

In summary, we developed a new acetamide/CPL-based eutectic solvent electrolyte with high solubilities over 1 M for all polysulfides and sulfide (K₂S_x, x=1–8) between 60 and 120 °C. Such high solubilities remarkably enhance ionic diffusion and reaction kinetics of K₂S₂ and K₂S, leading to AMS batteries with high energy density and low cost. Experimentally, a nearly theoretical discharge capacity of 1655 mAh g⁻¹ is achieved with 1 M sulfur in the catholyte at 75 °C, 2.6 times that with conventional TEGDME electrolytes. When the sulfur concentration further increases to 4 M, a high capacity of 830 mAh g⁻¹ is still delivered with 71 % capacity retention after 1000 cycles at 2 mA cm⁻² and 75 °C. Further energy density and economic analysis show that this new design has the potential to achieve a specific energy of 150–250 Wh kg⁻¹ at the cell level, and materials cost as low as ~\$30 kWh⁻¹ under weekly operation. Such performances are promising for long-duration energy storage.

Methods

Materials preparation

All chemicals were of analytical grade purity. For the CPL/acetamide mixture, one mole each of ε-caprolactam (CPL, 99% purity, Sigma Aldrich) and acetamide (99% purity, Sigma Aldrich) were dried at 50 °C within an argon-filled glovebox overnight prior to use. Subsequently, the two compounds were mixed and stirred at 50 °C for 30 min. Then, it was rested in a vacuum oven at 60 °C overnight to eliminate any trapped gas.

To form a catholyte, 0.125 M/0.5 M/1 M of anhydrous Na₂S (98%, Sigma Aldrich), 0.5 M potassium bis(trifluoromethanesulfonyl)imide (KTFSI, 97%, Sigma Aldrich), and 1.25 wt% (of solvent) Super C65 carbon black were mixed with CPL/acetamide and stirred at 80 °C until a homogeneous mixture was formed. Then a suitable amount of sulfur was added and stirred at 80 °C to form CPL/acetamide-based catholyte with different concentrations of [S]. TEGDME catholytes were prepared by the same procedure except that TEGDME was used instead of CPL/acetamide.

For the K-Na alloy anode, 0.01 mol potassium (98%, Sigma Aldrich) was mixed with 0.01 mol sodium (99.8%, Sigma Aldrich) in an aluminum container in an argon-filled glovebox. The liquid alloy was then combined with 1.25 wt% C65 carbon black, followed by stirring for 20 min.

Solubility test

The solubility of K₂S_x in electrolytes was evaluated using the following procedure: First, K₂S (Thermal Fisher Scientific) was mixed with sulfur with a 1:x molar ratio in a glass vial containing 500 μL of solvent. The mixture was then stirred on a hot plate set to a specific temperature. If

the solution became clear, then additional K₂S and sulfur would be added in the 1:x molar ratio. Otherwise, an additional amount of solvent was added. This process was repeated until the following conditions were met: first, a certain concentration, C₀, of K₂S_x was found to be soluble, as defined by the absence of solid in the vial after at least 2 h of sedimentation; second, C₀ + 0.05 M was not soluble, as indicated by the presence of solid precipitates after 2 hours. Once these conditions were satisfied, the solubility of K₂S₂ at the given temperature was considered to be C₀.

Cell assembly

CR2032 coin cells were used for cell assembly. Potassium-β"-alumina (K-BASE) with 1 mm thickness was purchased from Ionotec Inc. and cut into disks with 15 mm diameter. For Na-K symmetric cells, stainless steel foil was cut into round disks to fit the size of O rings. Then a thin layer of K-Na alloy with carbon black was coated on it. The components were then stacked in the following order: Anode case, 0.2 mm SAE-316L stainless steel spacer, wave disk spring, stainless steel foil, PTFE O-ring, K-BASE disk, PTFE O-ring, stainless steel foil, wave disk spring, 0.2 mm stainless steel spacer and cathode case. Finally, the assembled cell was compressed at 800 psi using a hydraulic press.

For K-Na/BASE/S full cells, carbon paper (Fuel Cell Earth) was cut into round disks to fit the size of the O-rings. During the assembly process, 26.7 μL cm⁻² of catholyte was dispensed onto two layers of carbon paper. The components were then stacked in the same order as the K-Na symmetric cell, except that one K-Na electrode was replaced by catholyte-soaked carbon paper. The corresponding configuration is shown in Supplementary Fig. 13.

Electrochemical measurement

Galvanostatic cycling electrochemistry measurement was performed on Landt battery tester CT3002A. Electrochemical impedance spectroscopy test (EIS) was performed on Bio-logic VMP3, with frequency ranged from 0.01 Hz to 1 MHz and voltage amplitude of 10 mV. All cells were kept at 75 °C in convection drying ovens (MTI Corp.).

Molecular dynamics simulation

To assist in validating the experimental data we utilized Molecular Dynamics (MD) simulation to calculate relative free energy of different solutes (e.g., K₂S & K₂S₂) in the key solvents (e.g., CPL/acetamide solvent & TEGDME) and to examine the radial distribution function (RDF) for key atoms. Using the Maginn Force Field Archive (MAFFA)⁴⁸ we assigned the Generalized Amber Force Field (GAFF) parameters for each molecule and generated atomic charges using the Restrained Electrostatic Potential (RESP) method⁴⁸. We then created an equidistant box with significantly more solvent molecules than the analyte. We then began an MD simulation using the Groningen Machine for Chemical Simulations (GROMACS) package⁴⁹.

In GROMACS, we set up a series of simulations that slowly add interaction between the solute and solvent using a coupling factor, λ . We started with a separated system with no interaction ($\lambda=0$) and eventually reached a fully interacting environment ($\lambda=1$). Once this simulation series was complete, we would have the available data to calculate the relative free energy difference and RDF for key atoms in the solution. Using a type of program called alchemical analysis we calculated Thermodynamic Integration (TI) and Multistate Bennett Acceptance Ratio (MBAR) values^{50,51}. Similarly, we ran a GROMACS code to produce RDF values. More details can be found in Supplementary Note 3.

Scanning electron microscope (SEM) imaging and energy dispersive spectroscopy (EDS) element mapping

K-Na/S coin cells containing 0.125 M K₂S₈ (1 M sulfur) in either CPL/acetamide or TEGDME solvent were assembled and cycled in a 75 °C oven. K₂S₈ catholyte was formed by mixing K₂S (Thermal Fisher

Scientific) and S (Sigma Aldrich) with the stoichiometric ratio in either CPL/acetamide or TEGDME and stirred at a 75 °C heat plate overnight. KTFSI and carbon black were not added to the catholyte. After the cycling process, the cell was dissembled to retrieve carbon paper in the cathode side for characterization. For TEGDME cells, the carbon paper was washed in the sequence of TEGDME and acetone and then dried inside the glovebox. For CPL/acetamide cells, Kimwipe paper was used to absorb the remaining liquid. The sample was sealed in an aluminum pouch during transportation to the facility. The SEM imaging with EDS mapping was done by Zeiss Sigma VP SEM with a voltage of 15 eV.

X-ray Absorption near edge structure (XANES) element mapping

K-Na/S coin cells containing 0.125 M K₂S₈ (1 M sulfur) in either CPL/acetamide or TEGDME solvent were assembled and cycled in a 75 °C oven. KTFSI and carbon black was not added to the catholyte. After cycling process, the cell was dissembled to retrieve carbon paper in the cathode side for characterization. The sample was sealed in aluminum pouch during transportation to the facility.

The XANES mapping was done in Brookhaven National Lab (BNL) with the 8-BM technique. 200 pixels * 200 pixels 2D scanning was done and the data was then analyzed and turned into 2D image by PyXRF software.

Operando optical microscopy and Fourier transform infrared (FTIR) spectroscopy

K-Na/S coin cells containing 0.0625 M K₂S₈ (0.5 M sulfur) in either CPL/acetamide or TEGDME solvent were assembled. O-shaped cathode cases (MTI Corp.) were employed to allow light transmission. For the cathode side, Kapton tape O-rings (Digikey) were used to replace PTFE O-rings. The cell images and videos were captured using NMM800TR metallurgical microscope in dark field and reflective modes. The discharge process for the cells was conducted by Bio-logic SP-5.

A Nicolet iS 5 FTIR Spectrometer was used to conduct FTIR experiments. The scanning range was from 400 to 4000 cm⁻¹, and the spectrum resolution was 4 cm⁻¹.

Data availability

The authors declare that the data supporting this study's findings are available within the paper and its supplementary information files. Source data are provided in this paper.

References

1. Bauer, C. et al. Charging sustainable batteries comment. *Nat. Sustain.* **5**, 176–178 (2022).
2. Wang, K. L. et al. Lithium-antimony-lead liquid metal battery for grid-level energy storage. *Nature* **514**, 348 (2014).
3. Hernandez, R. R. et al. Techno-ecological synergies of solar energy for global sustainability. *Nat. Sustain.* **2**, 560–568 (2019).
4. Dowling, J. A. et al. Role of long-duration energy storage in variable renewable electricity systems. *Joule* **4**, 1907–1928 (2020).
5. Sepulveda, N. A., Jenkins, J. D., Edington, A., Mallapragada, D. S. & Lester, R. K. The design space for long-duration energy storage in decarbonized power systems. *Nat. Energy* **6**, 506–516 (2021).
6. Hunter, C. A. et al. Techno-economic analysis of long-duration energy storage and flexible power generation technologies to support high-variable renewable energy grids. *Joule* **5**, 2077–2101 (2021).
7. Albertus, P., Manser, J. S. & Litzelman, S. Long-duration electricity storage applications, economics, and technologies. *Joule* **4**, 21–32 (2020).
8. Denholm, P., Cole, W., Frazier, A. W., Podkaminer, K. & Blair, N. *Storage Futures Study: The Challenge of Defining Long-Duration Energy Storage*. (United States, 2021).
9. Solomon, A. A., Kammen, D. M. & Callaway, D. The role of large-scale energy storage design and dispatch in the power grid: A study of very high grid penetration of variable renewable resources. *Appl. Energy* **134**, 75–89 (2014).
10. Whittacre, J. F. et al. An aqueous electrolyte, sodium ion functional, large format energy storage device for stationary applications. *J. Power Sources* **213**, 255–264 (2012).
11. Pham, V. H. et al. Selenium-sulfur (SeS) fast charging cathode for sodium and lithium metal batteries. *Energy Storage Mater.* **20**, 71–79 (2019).
12. Yang, F. et al. Sodium–sulfur flow battery for low-cost electrical storage. *Adv. Energy Mater.* **8**, 1701991 (2018).
13. Cheng, F., Liang, J., Tao, Z. & Chen, J. Functional materials for rechargeable batteries. *Adv. Mater.* **23**, 1695–1715 (2011).
14. Zhao, C. et al. Solid-state sodium batteries. *Adv. Energy Mater.* **8**, 1703012 (2018).
15. Lu, X., Xia, G., Lemmon, J. P. & Yang, Z. Advanced materials for sodium-beta alumina batteries: Status, challenges and perspectives. *J. Power Sources* **195**, 2431–2442 (2010).
16. Xu, Y., Jung, K., Park, Y.-C. & Kim, C.-S. Selection of container materials for modern planar sodium sulfur (NaS) energy storage cells towards higher thermo-mechanical stability. *J. Energy Storage* **12**, 215–225 (2017).
17. Lu, X. et al. Advanced intermediate-temperature Na–S battery. *Energy Environ. Sci.* **6**, 299–306 (2013).
18. Lu, X., Lemmon, J. P., Kim, J. Y., Sprenkle, V. L. & Yang, Z. High energy density Na–S/NiCl₂ hybrid battery. *J. Power Sources* **224**, 312–316 (2013).
19. Hueso, K. B., Armand, M. & Rojo, T. High temperature sodium batteries: status, challenges and future trends. *Energy Environ. Sci.* **6**, 734–749 (2013).
20. Liu, M. DEGRADATION OF SODIUM BETA'''-ALUMINA ELECTROLYTE IN CONTACT WITH SULFUR/SODIUM POLYSULFIDE MELTS. (1986).
21. Zhang, H. et al. Bidirectional tandem electrocatalysis manipulated sulfur speciation pathway for high-capacity and stable Na–S battery. *Angew. Chem.* **135**, e202217009 (2023).
22. Yang, T. et al. Design and construction of sodium polysulfides defense system for room-temperature Na–S battery. *Adv. Sci.* **6**, 1901557 (2019).
23. Wang, C. et al. Extending the low-temperature operation of sodium metal batteries combining linear and cyclic ether-based electrolyte solutions. *Nat. Commun.* **13**, 4934 (2022).
24. Wang, Y. et al. Revitalising sodium–sulfur batteries for non-high-temperature operation: a crucial review. *Energy Environ. Sci.* **13**, 3848–3879 (2020).
25. Wang, N. et al. High-performance room-temperature sodium–sulfur battery enabled by electrocatalytic sodium polysulfides full conversion. *Energy Environ. Sci.* **13**, 562–570 (2020).
26. Lee, B., Paek, E., Mitlin, D. & Lee, S. W. Sodium metal anodes: emerging solutions to dendrite growth. *Chem. Rev.* **119**, 5416–5460 (2019).
27. Wang, C. et al. Stable sodium–sulfur electrochemistry enabled by phosphorus-based complexation. *Proc. Natl. Acad. Sci. USA* **118**, e2116184118 (2021).
28. Yang, H. et al. Architecting freestanding sulfur cathodes for superior room-temperature Na–S batteries. *Adv. Funct. Mater.* **31**, 2102280 (2021).
29. Lei, Y. J. et al. Progress and prospects of emerging potassium–sulfur batteries. *Adv. Energy Mater.* **12**, <https://doi.org/10.1002/aenm.202202523> (2022).
30. Nikiforidis, G., Van de Sanden, M. & Tsampas, M. N. High and intermediate temperature sodium–sulfur batteries for energy storage: development, challenges and perspectives. *RSC Adv.* **9**, 5649–5673 (2019).

31. Lu, X. C., Bowden, M. E., Sprenkle, V. L. & Liu, J. A low cost, high energy density, and long cycle life potassium-sulfur battery for grid-scale energy storage. *Adv. Mater.* **27**, 5915–5922 (2015).
32. Hueso, K. B., Palomares, V., Armand, M. & Rojo, T. Challenges and perspectives on high and intermediate-temperature sodium batteries. *Nano Res.* **10**, 4082–4114 (2017).
33. El Jaroudi, O., Picquenard, E., Gobeltz, N., Demortier, A. & Corset, J. Raman spectroscopy study of the reaction between sodium Sulfide or disulfide and sulfur: Identity of the species formed in solid and Liquid Phases. *Inorg. Chem.* **38**, 2917–2923 (1999).
34. Zhao, Q., Hu, Y. X., Zhang, K. & Chen, J. Potassium-sulfur batteries: A new member of room-temperature rechargeable metal-sulfur batteries. *Inorg. Chem.* **53**, 9000–9005 (2014).
35. Nikiforidis, G., Jongerden, G. J., Jongerden, E. F., van de Sanden, M. C. M. & Tsampas, M. N. An electrochemical study on the cathode of the intermediate temperature tubular sodium-sulfur (NaS) Battery. *J. Electrochem. Soc.* **166**, A135 (2019).
36. Liu, Y. et al. Sulfur nanocomposite as a positive electrode material for rechargeable potassium-sulfur batteries. *Chem. Commun.* **54**, 2288–2291 (2018).
37. Ye, C. et al. Catalytic oxidation of KS via atomic Co and pyridinic N synergy in potassium-sulfur batteries. *J. Am. Chem. Soc.* **143**, 16902–16907 (2021).
38. Liu, B. Y., Zhao, J. J. & Wei, F. X. Characterization of caprolactam based eutectic ionic liquids and their application in SO₂ absorption. *J. Mol. Liq.* **180**, 19–25 (2013).
39. Guo, X. et al. Revealing the Solid-State Electrolyte Interfacial Stability Model with Na-K Liquid Alloy. *Angew. Chem. Int. Ed.* **61**, e202203409 (2022).
40. Lee, K., Kazyak, E., Wang, M. J., Dasgupta, N. P. & Sakamoto, J. Analyzing void formation and rewetting of thin in situ-formed Li anodes on LLZO. *Joule* **6**, 2547–2565 (2022).
41. Lu, X. et al. Liquid-metal electrode to enable ultra-low temperature sodium–beta alumina batteries for renewable energy storage. *Nat. Commun.* **5**, 4578 (2014).
42. Yang, Y. et al. High-capacity micrometer-sized Li₂S particles as cathode materials for advanced rechargeable lithium-ion batteries. *J. Am. Chem. Soc.* **134**, 15387–15394 (2012).
43. Shalygin, A. S., Milovanov, E. S., Yakushkin, S. S. & Martyanov, O. N. Chemical heterogeneity of deposits formed in the flocculant flow from crude oil, according to FTIR microscopy and chemical imaging. *Pet. Chem.* **61**, 1011–1018 (2021).
44. Darling, R. M., Gallagher, K. G., Kowalski, J. A., Ha, S. & Brushett, F. R. Pathways to low-cost electrochemical energy storage: a comparison of aqueous and nonaqueous flow batteries. *Energy Environ. Sci.* **7**, 3459–3477 (2014).
45. Zong, B. et al. Green production technology of the monomer of nylon-6: caprolactam. *Engineering* **3**, 379–384 (2017).
46. Duffner, F., Mauler, L., Wentker, M., Leker, J. & Winter, M. Large-scale automotive battery cell manufacturing: Analyzing strategic and operational effects on manufacturing costs. *Int. J. Prod. Econ.* **232**, <https://doi.org/10.1016/j.ijpe.2020.107982> (2021).
47. Liu, Y. T., Zhang, R. H., Wang, J. & Wang, Y. Current and future lithium-ion battery manufacturing. *Isience* **24**, <https://doi.org/10.1016/j.isci.2021.102332> (2021).
48. Zhang, Y., Squire, H., Gurkan, B. & Maginn, E. J. Refined classical force field for choline chloride and ethylene glycol mixtures over wide composition range. *J. Chem. Eng. Data* **67**, 1864–1871 (2022).
49. Berendsen, H. J., van der Spoel, D. & van Drunen, R. GROMACS: A message-passing parallel molecular dynamics implementation. *Comput. Phys. Commun.* **91**, 43–56 (1995).
50. Shirts, M. R. & Chodera, J. D. Statistically optimal analysis of samples from multiple equilibrium states. *J. Chem. Phys.* **129**, 124105 (2008).
51. Straatsma, T. & McCammon, J. Computational alchemy. *Annu. Rev. Phys. Chem.* **43**, 407–435 (1992).

Acknowledgements

Y.Y. acknowledges support from Columbia University, the Air Force Office of Scientific Research (FA9550-22-1-0226), and the program of Electrochemical Systems at the National Science Foundation (Award No. 2341994). Support from SEAS Interdisciplinary Research Seed (SIRS) and Climate School Seed Funding at Columbia University. T.M. thank Dr. Eliseo Marin Rimoldi for the discussion on MD simulations. This research uses 8-BM of the National Synchrotron Light Source II, a U.S. Department of Energy (DOE) Office of Science User Facility operated for the DOE Office of Science by Brookhaven National Laboratory under Contract No. DE-SC0012704.

Author contributions

Y.Y., D.L., and T.L. conceptualized the project, supervised the experiments, and contributed to the writing and revision of the manuscript, with Y.Y. serving as the principal supervisor. L.T. and Z.Y. designed and conducted the experiments, collected and analyzed data, performed characterization tests, and wrote the manuscript. S.Y., T. M., Q.C., S. R., W. Li., W. Lei., Y. C. Y., T. J., S. C., and J. W. assisted in the analysis and characterization of experimental data. Y. D. provided additional support and collaboration throughout the project.

Competing interests

The authors declare no competing interests.

Additional information

Supplementary information The online version contains supplementary material available at <https://doi.org/10.1038/s41467-024-51905-6>.

Correspondence and requests for materials should be addressed to Tengfei Luo, Donghui Long or Yuan Yang.

Peer review information *Nature Communications* thanks Maowen Xu and the other anonymous reviewers for their contributions to the peer review of this work. A peer review file is available.

Reprints and permissions information is available at <http://www.nature.com/reprints>

Publisher's note Springer Nature remains neutral with regard to jurisdictional claims in published maps and institutional affiliations.

Open Access This article is licensed under a Creative Commons Attribution-NonCommercial-NoDerivatives 4.0 International License, which permits any non-commercial use, sharing, distribution and reproduction in any medium or format, as long as you give appropriate credit to the original author(s) and the source, provide a link to the Creative Commons licence, and indicate if you modified the licensed material. You do not have permission under this licence to share adapted material derived from this article or parts of it. The images or other third party material in this article are included in the article's Creative Commons licence, unless indicated otherwise in a credit line to the material. If material is not included in the article's Creative Commons licence and your intended use is not permitted by statutory regulation or exceeds the permitted use, you will need to obtain permission directly from the copyright holder. To view a copy of this licence, visit <http://creativecommons.org/licenses/by-nc-nd/4.0/>.